Check for updates

Flexible pressure sensors with high pressure sensitivity and low detection limit using a unique honeycomb-designed polyimide/reduced graphene oxide composite aerogel†

Qiang Xu,[a] Xinhao Chang,[a] Zhendong Zhu,[a] Lin Xu,[a] Xianchun Chen,[b] Longbo Luo,*[a] Xiangyang Liu [ID][a] and Jiaqiang Qin [ID] *[a]

It is still a challenge to fabricate flexible pressure sensors that possess high sensitivity, ultralow detection limit, wide sensing range, and fast response for intelligent electronic devices. We here demonstrate superelastic and highly pressure-sensitive polyimide (PI)/reduced graphene oxide (rGO) aerogel sensors with unique honeycomb structure, which were designed and fabricated using a bidirectional freezing technique. This unique honeycomb structure with large aspect ratio is composed of aligned thin lamellar layers and interconnected bridges. The combination of the aligned lamellar layers and the bridges endows the aerogel sensors with high pressure sensitivity (1.33 kPa^{-1}), ultralow detection limit (3 Pa), broad detection range (80% strain, 59 kPa), fast response time (60 ms), and excellent stability during cycling (over 1000 cycles). Remarkably, the aerogel sensors maintain stable piezoresistive performance at -50 °C, 100 °C, and 200 °C in air, indicating promising potential applications in harsh environments. Owing to the high sensitivity and wide sensing range, the aerogel sensors have been used to detect a full-range of human motion including small-scale motion monitoring (wrist pulse, blowing, puffing) and large-scale movement monitoring (finger bending, elbow bending, walking, running). These advantages make the composite aerogels attractive for high-performance flexible pressure sensors and wearable electronic devices.

Introduction

High-performance flexible pressure sensors have attracted considerable research interests due to their wide applications in human motion detection, human–machine interaction, soft robotics, artificial skin, *etc.*[1-7] With the rapid development of flexible wearable electronic devices, sensor systems with integrated merits of high sensitivity, ultralow detection limit, wide sensing range, fast response, excellent recoverability and reproducibility, and environmental tolerance are urgently needed. Compared to pressure sensors based on piezoelectric,[8,9] triboelectric,[10] and capacitive[11,12] mechanisms, piezoresistive pressure sensors have attracted significant attention because of advantages such as simple preparation, low cost, and easy signal acquisition. Conventional piezoresistive pressure sensors made from metal[13] or semiconductor[14] materials have a high sensitivity, but show limited flexibility and small strain ranges

due to their intrinsic rigid structures, which hinders their applications for flexible electronic devices. Conductive elastomeric composites have been reported for flexible and wearable piezoresistive pressure sensors, which can detect resistance changes under high strain.[15,16] However, these sensors are insensitive, unstable, and difficult to detect low pressures (<10 kPa), limiting their practical applications in delicate sensing devices where high sensitivity and low detection limit are required.

Recently, porous conductive polymer composites (CPCs) have emerged as promising materials for piezoresistive pressure sensors due to a combination of lightweight, flexibility, and high compressibility. Porous CPCs are constructed *via* mixing conductive materials and polymer components, followed by a freeze-drying process;[17-20] neat conductive sponges impregnated with elastic polymer;[21,22] and solution dip coating of conductive nanomaterials on the backbone of nonconductive polymer sponges[23-26] have been used as flexible pressure sensors. Yang *et al.* prepared a polyimide-based graphene foam by dip-coating a polyimide foam template.[23] The foam possessed an interconnected cellular-like structure with continuous micropores. By controlling the dip-coating times, the foam achieved a pressure sensitivity of 0.36 kPa^{-1}. Wu *et al.*
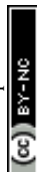
fabricated versatile pressure sensors based on microcrack-designed carbon black (CB)@polyurethane (PU) sponges *via* layer-by-layer assembly.[24] The CB@PU sponge owned an interconnected cellular-like structure with individual backbones, showing a sensitivity of 0.068 kPa^{-1}. Those pressure sensors with interconnected cellular-like structure usually exhibit relatively low pressure sensitivity and high detection limit due to small deformation and insufficient contact between conductive fillers under small external compression force, which hinders their applications in many delicate electronic devices. The sensing mechanism of piezoresistive pressure sensors is based on the change in resistance caused by the variation of contact area under compressive force. Thus, pressure sensitivity depends on the variation rate of conductive contact area under external pressure. A sensor with a certain physical structure causes a large compression deformation and a sharp increase of conductive contact area under a small compression force, ultimately greatly improving the sensitivity and decreasing the detection limit. However, highly pressure-sensitive sensors based on microstructure design are rarely explored by far. Besides sensitivity and detection limit, piezoresistive stability is also an important parameter of pressure sensors. Excellent mechanical elasticity and high compressibility are essential requirements for flexible pressure sensors to possess superior piezoresistive stability. Liu *et al.* reported lightweight and highly compressible carbon nanotube (CNT)/thermoplastic polyurethane (TPU)[19] and graphene/TPU[20] porous composites by a common freeze-drying technique. The disordered cellular-like structure of these composites can be easily subjected to destruction during compression cycles, causing irreversible plastic deformation and deterioration in the electrical conductivity and sensitivity. In recently, Huang *et al.* designed a CNT/TPU foam with an aligned porous structure *via* a directional freezing method.[27] The aligned CNT/TPU foams exhibit better compression recovery ability than those of the disordered CNT/TPU foams, achieving a superior piezoresistive recoverability and reproducibility. Hence, rational microstructure design is an effective approach to improve the sensitivity, decrease the detection limit, and achieve excellent piezoresistive stability of pressure sensors.

For certain applications, such as household appliances and aerospace, pressure sensors with excellent high temperature tolerance are highly desired. Flexible chain polymers, such as PU, are widely used in pressure sensors.[24–29] However, these PU-based pressure sensors usually suffer from poor thermal and structural stability at elevated temperatures, limiting their application in high temperature environment. In addition, the obvious creep and hysteresis of flexible chain polymers are not desirable for the cyclic stability and rapid response of pressure sensors. Owing to the flexibility, excellent mechanical performance, high/low-temperature tolerance, chemical and radiation resistance,[30,31] PI with rigid chain structure is a more ideal polymer matrix for fabrication of pressure sensors with fast response, superior piezoresistive stability, and excellent tolerance to harsh environments.

In this article, we design and fabricate a flexible pressure sensor using superelastic and highly pressure-sensitive PI/rGO composite aerogels with unique honeycomb structure *via* a bidirectional freezing technique. This unique honeycomb structure with large aspect ratio composed of aligned thin lamellar layers and interconnected bridges was achieved through a proper control of nucleation and growth of ice crystals under bidirectional temperature gradients. Due to the large aspect ratio honeycomb structure and thin pore wall of PI/rGO aerogel, a small variation in pressure can cause significant deformation of the aerogel, resulting in closer contacts of the parallel lamellar layers and generating dramatically more conductive pathways, which enables high pressure sensitivity (1.33 kPa^{-1}), ultralow detection limit (3 Pa), and fast response time (60 ms). Besides, the integration of the aligned lamellar layers and the bridges is beneficial for achieving high compressibility and superior superelasticity, endowing the pressure sensor with wide sensing range (80% strain, 59 kPa), excellent piezoresistive recoverability and reproducibility (over 1000 cycles). Graphene is used as the conductive filler due to its extremely high electrical conductivity, excellent mechanical flexibility, large specific surface area, and thermal and chemical stability.[32,33] Here, water-soluble PI precursor polyamic acid salt (PAAS) can form a strong interfacial interaction with GO, promoting the uniform dispersion of GO in aqueous solution, which is the prerequisite for the preparation of high-performance composite aerogels. Due to the excellent low temperature resistance and thermal stability, we have explored the sensing performance of the composite aerogels at −50 °C, 100 °C, and 200 °C in air, while most commercial polymer foams cannot maintain their structural integrity under the same condition. Finally, pressure sensors were attached to various parts of the human body to detect full-range human motions. These superior comprehensive sensing properties enable the PI/rGO aerogels for wide potential applications in human health monitoring, artificial intelligence, artificial skin, *etc.*

Experimental section

Materials

N,N-Dimethylacetamide (DMAc), triethylamine (TEA, 99%), deionized water, acetone, KMnO$_4$, H$_2$SO$_4$ (98%), NaNO$_3$, H$_2$O$_2$, and HCl were acquired from Chengdu Kelong Chemical Reagent Co., Ltd. Pyromellitic dianhydride (PMDA) and 4,4′-oxidianiline (ODA) were purchased from Changzhou Sunlight Medical Raw Material Co., Ltd.

Preparation of water-soluble polyamic acid salt (PAAS) powder

The procedure was as follows: the ODA was dispersed in DMAc using a mechanical stirrer. After the ODA was dissolved, PMDA was added into the mixture by mechanically stirring for 6 h in an ice bath to obtain viscous polyamic acid (PAA) solution. The PMDA/ODA molar ratio was 100 : 99. Subsequently, triethylamine (TEA) was added to the PAA solution and stirred for another 2 h to obtain the more viscous PAAS solution. And the molar ratio of TEA to carboxyl groups in PAA was 1 : 1. Next, PAAS was precipitated in the form of powder after acetone was slowly dropped to the solution. And the precipitate was washed

by acetone several times. Finally, the PAAS powder was obtained by vacuum filtration and vacuum drying at 45 °C for 6 h.

Preparation of PI/rGO composite aerogels

GO was prepared by the modified Hummers method.[34] The PI/rGO composite aerogels were fabricated by bidirectional freeze casting, freeze-drying, and thermal annealing. Typically, PAAS powder (1 g) was added to 49 g of deionized water, and a PAAS solution with 2% solid content was prepared. Then, 100 mg of GO was dispersed into the above solution using ultrasonication at 200 W for 30 min, achieving a homogeneous PAAS/GO dispersion. Next, the mixture was transferred into the bidirectional freezing device for freeze casting. After completely freezing, the sample was dried in a lyophilizer (−53 °C, 10 Pa) for 36 h to get the PAAS/GO aerogels. Then, these dried PAAS/GO aerogels were heated under vacuum at 100 °C, 200 °C, 250 °C and 400 °C for 1 h, 1 h, 1 h and 0.5 h, respectively to obtain PI/rGO-10 aerogels. Similarly, a series of PI/rGO aerogels were prepared by changing the GO loading, and the PI/rGO aerogels with mass ratios (PAAS to GO) of 100 : 5, 100 : 10 and 100 : 15 were denoted as PI/rGO-5, PI/rGO-10 and PI/rGO-15, respectively. In addition, the neat PI aerogel was also prepared using the same procedure without GO.

Characterization

The microstructure of the aerogels was investigated using a FEI Inspect F (FEI Company, EU/USA) scanning electron microscopy (SEM). Fourier transform infrared (FT-IR) spectra in the range of 600–4000 cm^{-1} were obtained using Nicolet 5700 FT-IR spectrometer. Raman spectra were recorded using a Raman spectrometer (HORIBA Lab RAM HR Evolution) with a laser excitation of 532 nm. Thermal stability was conducted using a thermogravimetric analysis (TGA) instrument (NETZSCH TG209F1) under a nitrogen flow from 30 °C to 800 °C at a heating rate of 10 °C min^{-1}. AXIS Ultra DLD (Kratos, UK) apparatus was used for X-ray photoelectron spectroscopy (XPS) analysis. Compressive tests were performed using an Instron Corporation 5967 universal testing machine with a 500 N load cell. The slope of the initial linear portion of stress–strain curve is used as the compressive modulus. And compressive stress at 50% strain was used as compressive strength. In order to test the electrical performance of our sensors, the composite aerogel was sandwiched between two copper plates using polyimide tape, and silver paste was used to ensure good electrical contact between them. Then, a Keithley 2601B source meter (USA) coupled with universal testing machine was used to investigate the piezoresistive performance of the composite aerogels.

Results and discussion

As shown in Fig. 1a, the PI/rGO composite aerogels were fabricated by mixing PAAS and GO in aqueous solution, bidirectional freeze casting, freeze-drying, and thermal annealing. The strong interfacial interaction between the water-soluble PAAS molecules and GO is crucial for promoting the uniform dispersion of GO, forming a mechanically robust structure. PAAS/GO solution

was poured into a cubic Teflon mold placed on the surface of a bent copper plate with one end immersed in liquid nitrogen (−196 °C) and the other end exposed to air (25 °C) to induce horizontal (ΔT_x) and vertical (ΔT_z) temperature gradients. Under such conditions, ice crystals nucleated only in the y-axis direction, and grew preferentially along horizontal direction (x-axis) to form parallel ice columns. The growing parallel ice columns were interrupted by PAAS/GO molecules in the initial freezing process. These interrupted parallel ice columns simultaneously grew along vertical direction (z-axis) to form long-range interrupted parallel ice lamellae. Meanwhile, PAAS/GO was phase separated from ice and aggregated between the interrupted parallel ice lamellae. After freeze-drying and thermal annealing, PI/rGO composite aerogels with aligned large aspect ratio honeycomb structure were obtained. Thermal annealing of the PAAS/GO composite aerogels converts the PAAS to PI and causes the reduction of GO. As described in Experimental section, the samples with different rGO loadings are designated as PI/rGO-5, PI/rGO-10, and PI/rGO-15. The sample used for characterization is the PI/rGO-10 composite aerogel, unless otherwise described. The neat PI aerogel was also prepared for comparison. Scanning electron microscopy (SEM) was conducted to characterize the morphologies of the PI/rGO-10 aerogel and the neat PI aerogel. Owing to the bidirectional freezing fabrication process, the PI/rGO-10 aerogel and the neat PI aerogel show large-scale aligned lamellar microstructure in yz cross section (Fig. S1a and b†). As shown in Fig. 1b and c (xy and yz cross-sections, respectively), the PI/rGO-10 aerogel exhibits large aspect ratio honeycomb structure composed of aligned thin lamellar layers and interconnected bridges. The aspect ratio of this unique honeycomb structure is generally larger than 5 : 1 (3 : 1 to 15 : 1), which is much higher than that of typical honeycomb structure (around 1 : 1). Bridges between lamellar layers may arise from the interruption of the growing ice columns in the initial freezing process, and the interrupted ice columns then grow into interrupted ice lamellae with PAAS/GO trapped between them. The presence of the bridges helps to promote the compression recovery and improve the cyclic compression stability. The pore wall thickness of the PI/rGO-10 aerogel and the neat PI aerogel is about hundreds of nanometers (Fig. S1c and d†). Large aspect ratio honeycomb structure and thin pore wall enable large compression deformation under small external force, resulting in high sensitivity and low detection limit for the PI/rGO-10 sensor. Compared to the smooth pore wall of the neat PI aerogel, the PI/rGO-10 aerogel shows wrinkled and rough pore wall structure, indicating the successful attachment of graphene sheets on the PI skeleton. As shown in Fig. 1d and e, the aerogel exhibits a normal honeycomb structure without the horizontal temperature gradient. Therefore, the bidirectional temperature gradients are essential for the formation of this unique honeycomb structure. Fig. S2† shows the variation of the samples during the fabrication process of the neat PI aerogel and the PI/rGO-10 aerogel. The neat PI aerogel exhibits a large shrinkage as high as 55.2%, while the PI/rGO-10 aerogel displays a small shrinkage of 23.5% due to the strong interactions between rGO and PI. As a result, the PI/rGO-10 aerogel shows a density of only

24.1 mg cm^{-3}. The integration of PI and rGO is beneficial for sustaining the integrity and stability of the porous structure during cyclic compression. The PI/rGO-10 aerogel can withstand a compression strain as high as 90% without structure degradation and recover back to its initial state immediately after release of the external stress (Fig. 1f and Movie S1†), showing outstanding structural robustness, excellent compressibility and recoverability.
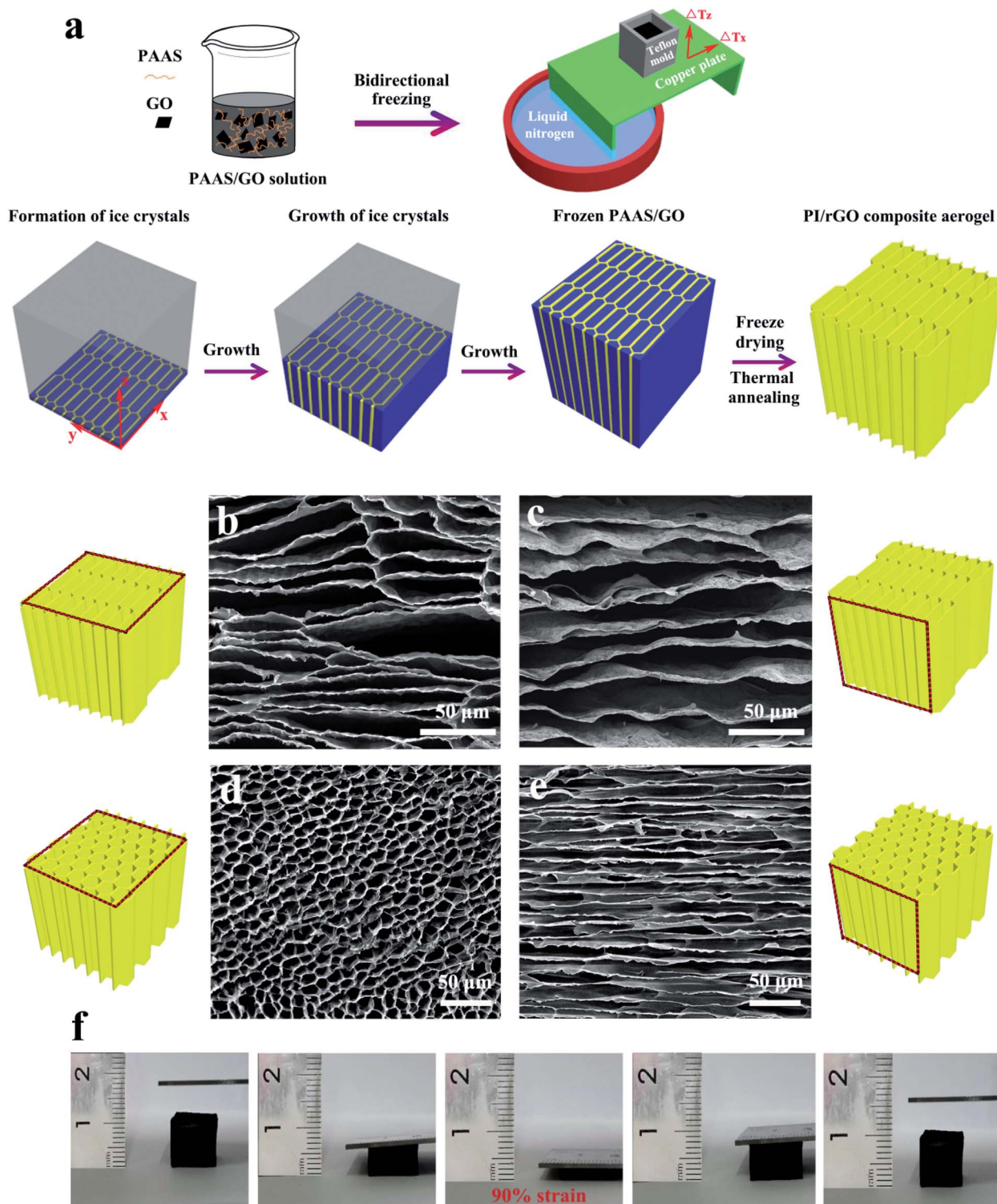
Fig. 1 (a) Schematic illustration of the bidirectional freezing fabrication process. (b and c) SEM images of a PI/rGO-10 aerogel showing the *xy* and *yz* cross-sections, respectively. (d and e) SEM images of a PI/rGO-10 aerogel without the horizontal temperature gradient showing the *xy* and *yz* cross-sections, respectively. (f) Photographs of compression–recovery process of a PI/rGO-10 aerogel.

Fourier transform infrared (FT-IR) spectroscopy, Raman spectroscopy, and X-ray photoelectron spectroscopy (XPS) were conducted to evaluate the chemical structure and interactions between rGO and PI. As shown in Fig. 2a, the FT-IR spectra of GO exhibits two prominent characteristic peaks at 3401 cm^{-1} and 1624 cm^{-1}, corresponding to the O–H and aromatic C=C stretching vibrations. In the case of rGO, the peak intensities for the oxygen-containing groups decrease, reflecting GO was reduced during thermal annealing. In the FT-IR spectrum of the PI aerogel, the peaks at 1726 cm^{-1} and 1776 cm^{-1} are attributed to imide C=O symmetric and asymmetric stretching vibrations, respectively. Meanwhile, C–N stretching vibration and C=C stretching vibration are observed at 1377 cm^{-1} and 1505 cm^{-1}, respectively.[35] As for PI/rGO aerogel, the absorption peaks of C=O, C=C, and C–N stretching vibrations are shifted to the lower wavenumbers compared to PI aerogel, which indicates the strong hydrogen bond interaction between PI and rGO (Fig. S3†). The Raman spectra are presented in Fig. S4,† two prominent characteristic peaks of the rGO sample are around 1346 and 1585 cm^{-1} respectively, corresponding to the D-band and G-band of graphitic carbon. For the PI sample, the peaks at 1386 and 1610 cm^{-1} indicate the C–N stretching vibration of the imide ring and aromatic imide ring vibration of the dianhydride portion, respectively. In the PI/rGO composite aerogel, the two adjacent characteristic peaks of PI and rGO overlap to form broad vibration peaks at 1348 and 1599 cm^{-1}, respectively, which are mainly attributed to the charge transfer between PI

and rGO. X-ray photoelectron spectroscopy (XPS) measurement was conducted to further determine the variation of elemental composition. The C 1s spectrum of rGO consist of three components at 284.6 eV (C=C/C–C), 286.6 eV (C–O), and 287.8 eV (C=O) (Fig. 2c). The peak intensity of C–C for rGO increases compared with that for GO, while the peaks for oxidation groups decrease sharply.[36] And the increase of C/O atomic concentration ratio further confirms the reduction of GO during the thermal annealing process (Table S1†). Fig. 2b shows that both PI and PI/rGO contain significant peaks of C 1s (284.6 eV), N 1s (400 eV), and O 1s (532 eV).[37] Due to the existence of rGO, the PI/rGO aerogel exhibits lower N and O percentages and higher C percentage compared to the neat PI aerogel (Fig. 2b and Table S1†). Four configurations centering at 284.6 eV (C=C/C–C), 285.5 eV (C–N), 286.3 eV (C–O), and 288.6 eV (C=O) can be observed in the C 1s spectra of PI (Fig. 2c).[38] Compared with PI, the peak intensities for C–N, C–O and C=O of PI/rGO decrease, while the peak intensity of sp^2 carbon increase, indicating strong interactions between PI and rGO. Thermal stability of GO, rGO, PI and PI/rGO aerogels were characterized with TGA (Fig. 2d). The onset decomposition temperature (the temperatures at 5% weight loss, $T_{5\%}$) of rGO is at around 385 °C, and there is 79% weight retention until 800 °C, showing higher thermal stability than GO (Fig. S5†). This result further confirms the reduction of GO during the thermal annealing process. Compared with rGO, the PI/rGO aerogel exhibits an increase in onset decomposition
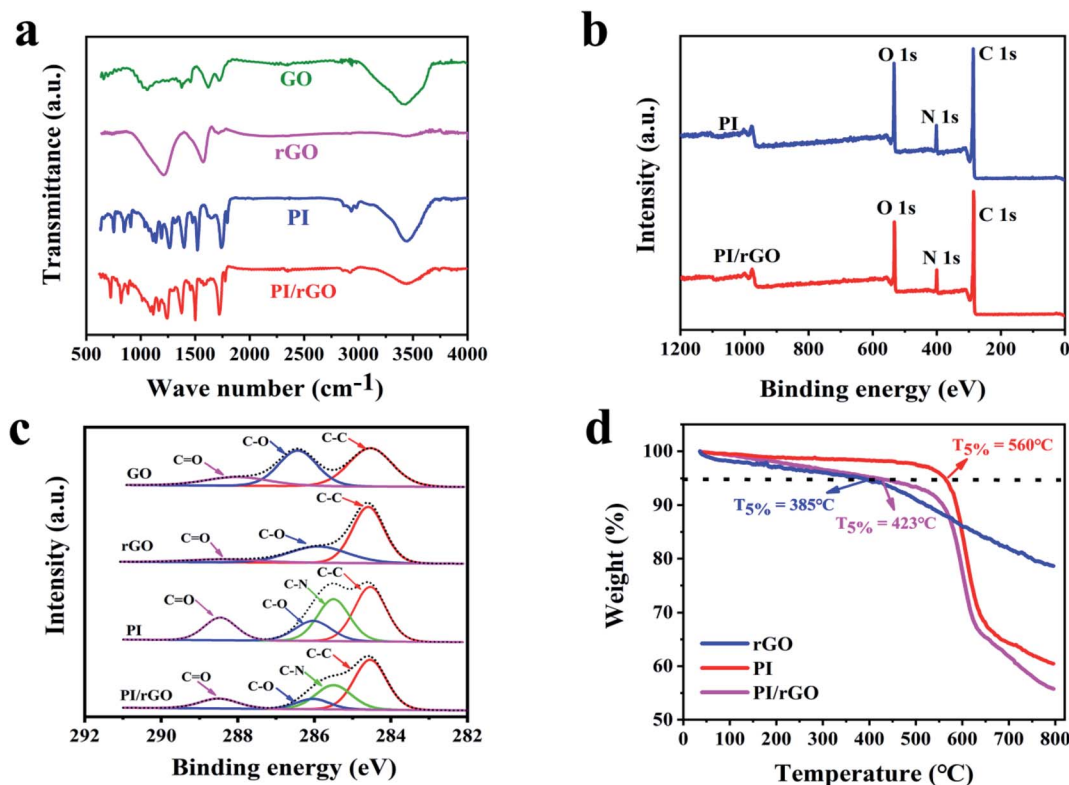

Fig. 2 (a) FT-IR spectra for GO, rGO, PI, and PI/rGO. (b) XPS spectra for PI and PI/rGO. (c) C 1s spectra for GO, rGO, PI, and PI/rGO. (d) TGA curves for rGO, PI and PI/rGO.

View Article Online

temperature due to the strong interaction between PI and rGO. The PI/rGO aerogel possesses lower thermal stability than that of PI aerogel, which can be ascribed to the rGO acts as a heat source to induce decomposition of PI. Nevertheless, the onset decomposition temperature of the PI/rGO aerogel is still up to 423 °C, indicating outstanding thermal stability.

To obtain the mechanical performance of the PI/rGO aerogels, a set of compressive tests were conducted. The stress–strain (σ–ε) curves of different PI/rGO aerogels with 80% compression strain are shown in Fig. 3a. The compression strength is defined as the compression stress at 50% strain. Fig. 3b shows that the compression modulus and strength are significantly enhanced with increasing rGO loading due to the strong interactions between rGO and PI, indicating the mechanical properties could be effectively adjusted to meet different application requirements. The loading stress–strain curve of PI/rGO aerogels could be divided into three characteristic stages: a linear region up to 40% due to the elastic deformation of the cell walls, a plateau region for 40% < ε < 60%, and a densification region for ε > 60% with compressive stress increased dramatically due to densification of the porous structure. The cyclic stress–strain curves of PI/rGO-5, PI/rGO-10, and PI/rGO-15 aerogels in 100 loading–unloading cycles with 50% strain are shown in Fig. 3c–e. These three different composite aerogels exhibit no significant plastic deformation and stress reduction over the 100 cycles, which implies their structural robustness and excellent fatigue resistance. Furthermore, during 100 fatigue cycles, the energy loss coefficient (the ratio of the hysteresis loop area to the area under the loading curve)[18] slightly decreases and gradually stabilizes (Fig. 3c–e, inset), indicating minor structural change during cyclic compression. Fig. S6† compares the stress reduction *versus* plastic deformation for the PI/rGO-10 aerogel and other previously reported porous materials. The PI/rGO-10 aerogel maintains 99.6% of the maximum stress and suffers only 1% plastic deformation after 100 compression cycles for 50% strain,
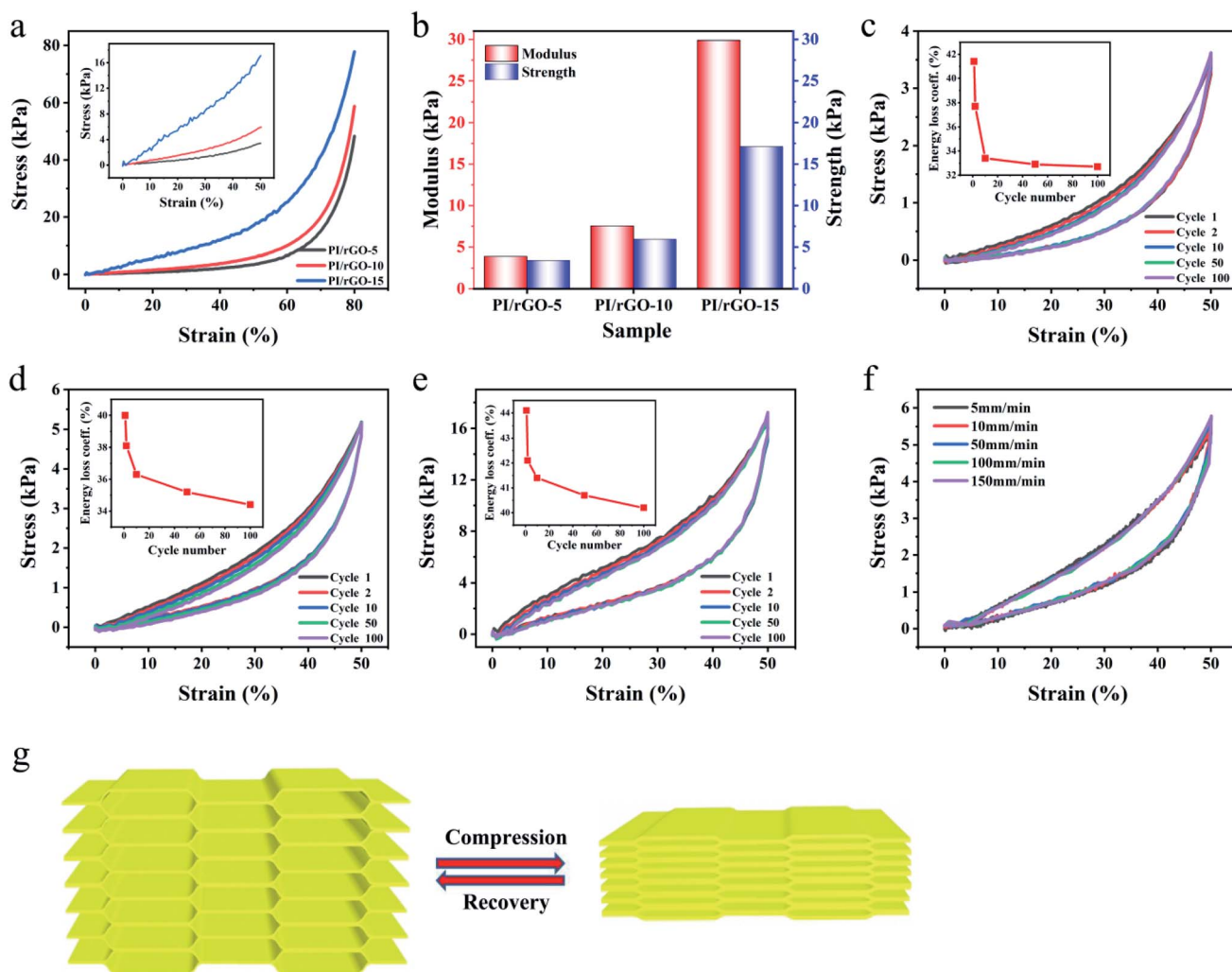
Fig. 3 (a) The stress–strain (σ–ε) curves and (b) compression modulus and strength for PI/rGO aerogels with different GO loadings. Inset: stress–strain (σ–ε) curves for 50% strain. (c–e) Fatigue tests for PI/rGO-5, PI/rGO-10, and PI/rGO-15 aerogels using 50% strain for 100 cycles. Inset: energy loss coefficients over 100 cycles. (f) Stress–strain curves for a PI/rGO-10 aerogel using different strain rates. (g) Schematic of the compression–recovery process of PI/rGO aerogels.
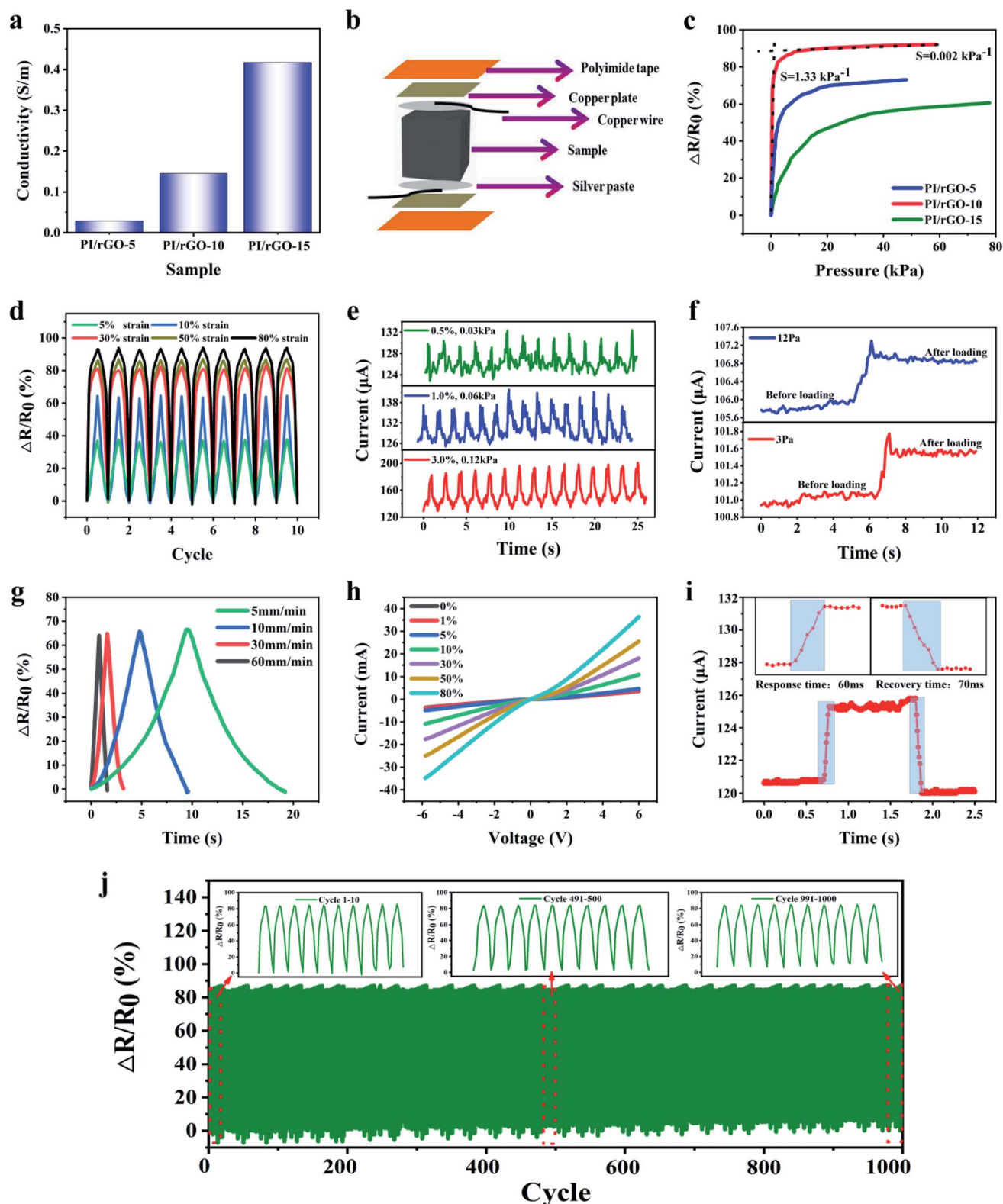
Fig. 4 (a) The electrical conductivity for different PI/rGO aerogels. (b) The fabrication process for a PI/rGO pressure sensor. (c) $\Delta R/R_0$ as a function of pressure. (d and e) Cyclic response curves for a PI/rGO-10 sensor using different compression strains. (f) Detection limit test for a PI/rGO-10 sensor. (g) $\Delta R/R_0$ for a PI/rGO-10 sensor using different compressive rates for 10% strain. (h) $I-V$ curves for a PI/rGO-10 sensor using different compression strains. (i) Response time and recovery time for a PI/rGO-10 sensor with 0.5% strain at a speed of 250 mm min^{-1}. (j) Piezoresistive recoverability and reproducibility tests for a PI/rGO-10 sensor using a 50% compression strain for 1000 cycles.

indicating more superior elasticity and fatigue resistance compared with compressible carbon aerogels or sponges,[39,40] and porous composite aerogels or foams.[41–45] Besides, the stress–strain curves of the PI/rGO-5, PI/rGO-10, PI/rGO-15 aerogels at different strain rates (5–150 mm min^{-1}) almost overlap, indicating that the composite aerogels can maintain excellent compression stability even under rapid deformation (Fig. 3f and S7†). Finally, we use a compression–recovery schematic to clarify the influence of the microstructure on the mechanical properties (Fig. 3g). Large-scale aligned lamellar structure is favorable for spreading loads to avoid stress concentration, preventing local damage of the structure. Furthermore, the bridges act as numerous springs to maintain structural integrity and promote elastic deformation and strength recovery. The combination of the aligned lamellar layers and the bridges endows the composite aerogels with high compressibility, excellent elasticity and fatigue resistance. After compression, the composite aerogels can recover to its original state without significant degradation.

The effects of rGO loading on the electrical conductivity of the composite aerogels were studied. The electrical conductivity increases with increasing rGO loading (0.029 S m^{-1} for PI/rGO-5, 0.145 S m^{-1} for PI/rGO-10, 0.417 S m^{-1} for PI/rGO-15), because more conductive pathways are generated with higher rGO loading (Fig. 4a). The merits of lightweight, excellent elasticity and conductivity make PI/rGO aerogels suitable for applications as flexible pressure sensors. Fig. 4b illustrates the fabrication process of a piezoresistive PI/rGO pressure sensor. The composite aerogel was sandwiched between two copper plates using polyimide tape, and silver paste was used to ensure good electrical contact to obtain a stable signal output. To demonstrate the pressure sensitivity of the composite aerogels, the resistance variation ratio ($\Delta R/R_0 = (R_0 - R_t)/R_0$, where R_0 and R_t are the resistances without and with applied pressure, respectively) *versus* the applied pressure was investigated (Fig. 4c). The pressure sensitivity (S) is defined as $S = \delta(\Delta R/R_0)/\delta P$.[25] The contacts of the adjacent aerogel cell walls upon external compression force lead to an increase in conductive pathways and a decrease in resistance. The results show that PI/rGO-10 sensor provides higher pressure sensitivity than PI/rGO-5 and PI/rGO-15. This is mainly due to the PI/rGO-5 sensor does not have sufficient conductive fillers to generate more

conductive contacts during compression, so the sensitivity is limited. As for the PI/rGO-15 sensor, the excess addition of rGO will significantly increase initial conductivity, in return affecting its further increase of conductive pathways, resulting in the small resistance variation ratio. The PI/rGO-10 sensor possesses optimal amount of rGO to form new conductive pathways, the resistance decreases sharply under external pressure, showing a more sensitive piezoresistive response behavior. The sensitivity curve of PI/rGO-10 sensor shows two characteristic stages corresponding to differences in sensitivity. In the low pressure regime (0–0.52 kPa), sensitivity curve exhibits a large slope with a high sensitivity of 1.33 kPa^{-1}. Due to the low modulus of the PI/rGO-10 sensor, a small variation in pressure leads to significant structure deformation, and the conductive contact area increases sharply, causing a dramatic increase in $\Delta R/R_0$. While in the large pressure regime (20–59 kPa), the sensitivity decreases to 0.002 kPa^{-1}. The conductive contact points approach saturation because of the densification of the aerogel, leading to lower pressure sensitivity. These results also indicate that the PI/rGO-10 sensor has a wide sensing range (80% strain, 59 kPa). The cyclic response behavior of the PI/rGO-10 sensor for different compression strains are shown in Fig. 4d and e. Notably, the change of current signal was effectively detected for strain as low as 0.5%, corresponding a pressure of 30 Pa. Moreover, stable and reproducible current signals were observed in a wide strain range. Stable piezoresistive response over a wide strain range enables the aerogel sensor for monitoring both tiny motions and large-scale human bodily movements. To determine the detection limit, we applied a pressure of 3 Pa on the PI/rGO-10 sensor (10 mm × 10 mm) by loading a cobalt silicone particle (30 mg). A small increase in electrical current (0.8 µA) was detected upon loading the cobalt silicone particle, which was due to the decrease in electrical resistance in response to the compression of the aerogel. Subsequently, the current slightly decreased and remained stable (Fig. 4f). When the applied pressure on the PI/rGO-10 sensor increased to 12 Pa, the corresponding increase in electrical current was 1.5 times that for the 3 Pa applied pressure. These results indicate that the PI/rGO-10 sensor exhibits ultralow detection limit (3 Pa), which is suitable for low-pressure measurement applications. Different compression speeds have minimal impact on the maximum $\Delta R/R_0$ due to the same final applied strain, which

Table 1 Summary of recently reported piezoresistive pressure sensors

| Material	Pressure sensitivity	Sensing range	Detection limit	Response time	Ref.
CB@PU sponge	0.068 kPa^{-1}	60% strain (16 kPa)	17 Pa	20 ms	24
Graphene/polyurethane sponge	0.26 kPa^{-1}	10 kPa	9 Pa	—	25
rGO/PI nanocomposite foam	0.18 kPa^{-1}	50% strain (6.5 kPa)	—	—	17
Au/PU sponge	0.122 kPa^{-1}	60% strain (14 kPa)	0.568 Pa	9 ms; 500 mm s^{-1}	28
MWNT–rGO@PU foam	0.088 kPa^{-1}	99% strain (50 kPa)	3.7 pa	30 ms	26
GO/PPy@PU sponge	0.79 kPa^{-1}	80% strain (15 kPa)	75 Pa	70 ms	29
PEDOT:PSS/PI aerogel	0.054 kPa^{-1}	70% strain (17 kPa)	—	—	45
PI/CNT aerogel	0.11 kPa^{-1}	0–80% strain (0–61 kPa)	<10 Pa	50 ms; 1000 mm min^{-1}	44
Polyimide-based graphene foam	0.36 kPa^{-1}	50% strain (15 kPa)	—	80 ms	23
rGO/PANi@melamine sponge	0.152 kPa^{-1}	27 kPa	—	96 ms	46
This work	1.33 kPa^{-1}	80% strain (59 kPa)	3 Pa	60 ms; 250 mm min^{-1}	
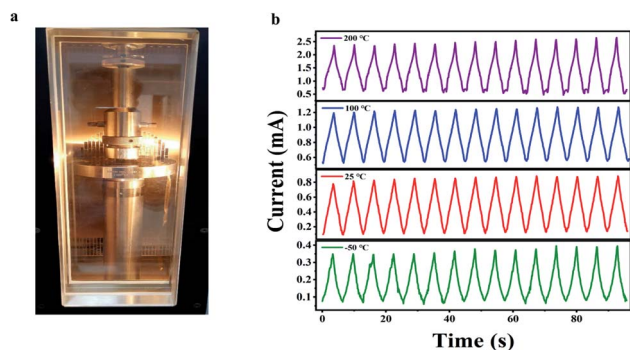
Fig. 5 (a) The high/low-temperature environment test system. (b) Cyclic piezoresistive response behaviors for a PI/rGO-10 sensor at different temperatures in air using 50% compression strain for 15 cycles.

is critical for the sensor stability in practical application (Fig. 4g). The current–voltage curves under different applied strains (0–80%) show nearly linear ohmic behaviors, indicating stable electrical property of the sensor (Fig. 4h). Our PI/rGO-10 sensor has very fast response time (60 ms) and recovery time (70 ms) for a compression speed of 250 mm min⁻¹ (Fig. 4i), which is capable of real-time monitoring of human body movements. Importantly, the resistance variation ratio of the PI/rGO-10 senor for 50% strain exhibited no distinguishable change for the investigated 1000 compression cycles (Fig. 4j), which likely results from the excellent elasticity and structural reversibility

of the composite aerogel. Table 1 compares the performance of the PI/rGO-10 pressure sensor in this work and the recently reported piezoresistive pressure sensors. Our PI/rGO-10 pressure sensor exhibits a pressure sensitivity up to 1.33 kPa⁻¹, which is higher than other similar pressure sensors.[17,23–26,28,29,44–46] Moreover, other important parameters of our PI/rGO-10 pressure sensor such as sensing range, detection limit, and response time are comparable to the reported pressure sensors.

It is still a challenge to fabricate polymer-based pressure sensors for applications in a wide temperature range. We explored cyclic piezoresistive response behaviors of the PI/rGO-10 sensor at −50 °C, 25 °C, 100 °C, and 200 °C under 50% compression strain for 15 cycles in air using a wide temperature environment test system (Fig. 5a). The PI/rGO-10 sensor maintained stable and reproducible current responses at different temperatures, implying outstanding sensing performance under harsh temperature conditions (Fig. 5b). In comparison, most commercial polymer foams cannot maintain their structural integrity under the same conditions. It is noted that the initial current increases with increasing temperature, possibly due to the negative temperature coefficient (NTC) effect of rGO. The thermal disturbance created by the temperature increase causes the variety of electric field between the graphene sheets, and the probability of electron transition increases, resulting in a decrease in resistivity.[47,48] When being compressively cycled between 0 and 50% strain at −50 °C in air, the PI/rGO-10 sensor maintains 98.5% of maximum stress and suffers only 2.8%
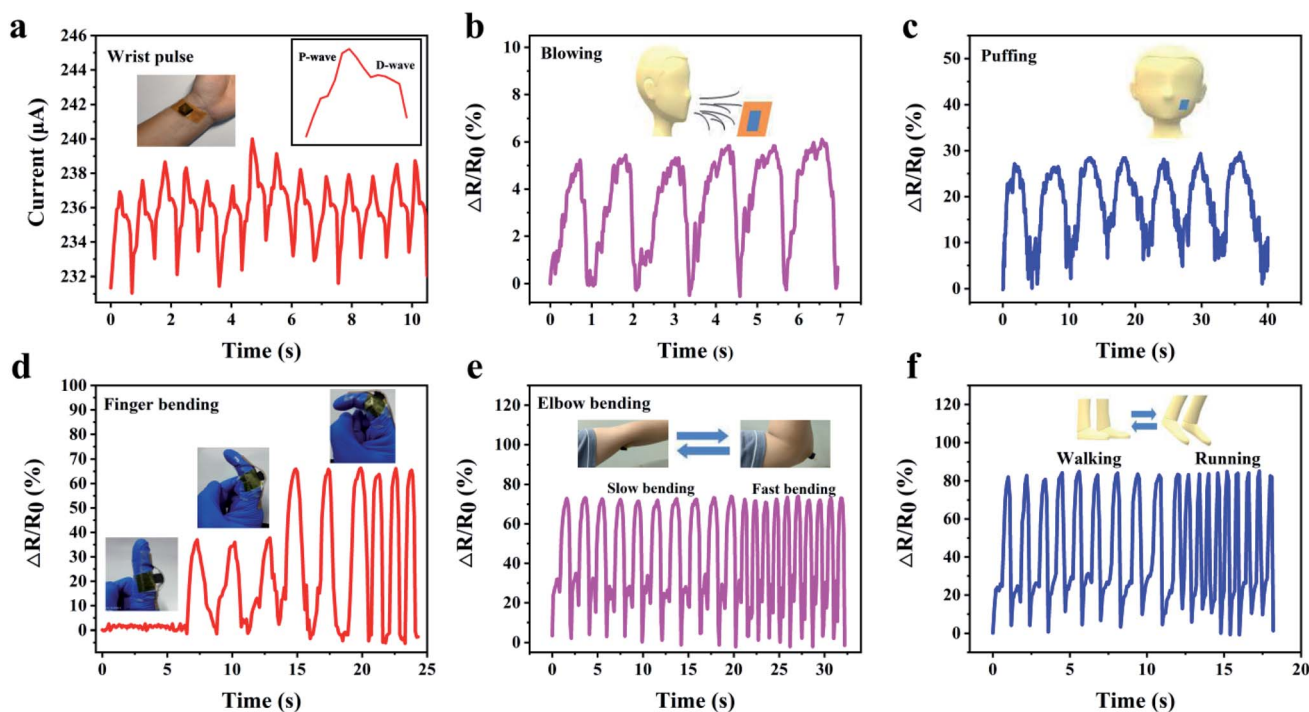

Fig. 6 (a) Monitoring of the wrist pulse in real-time by attaching a PI/rGO-10 sensor to a wrist; the inset shows a single pulse. (b) Monitoring real-time signal for blowing air on a PI/rGO-10 sensor. (c) Monitoring tiny face muscle motion caused by puffing. (d) Real-time signal recording for finger bending; the inset shows the bending degree. (e) Real-time signal recording for elbow bending. (f) Real-time signal recording for walking and running.

permanent deformation after 15 cycles (Fig. S8a and d†), indicating outstanding structural reversibility and stability of the pressure sensor in low temperature environment. For compressive cycling at 100 °C between 0 and 50% strain in air (Fig. S8b†), the maximum stress shows a slight decrease of 1.1%, and the height maintains 94.7% of original value (Fig. S8e†). Moreover, even at a high temperature of 200 °C (Fig. S8c†), the PI/rGO-10 sensor still retains over 92% of its maximum stress and shows only 9.2% plastic deformation (Fig. S8f†). These results indicate that our composite aerogels possess excellent structural stability in a wide temperature range, which enables stable sensing performance in harsh temperature environments.

For application in human motion detection, we evaluated the capabilities of our pressure sensor for various types of human motion detection. For small-scale human motion, a PI/rGO sensor was attached to a wrist to monitor the pulse in real-time (Fig. 6a). The result shows that the sensor can accurately record such a weak pressure change. And the percussion wave (P) and diastolic wave (D) of characteristic human pulse waveform can be clearly identified from a single wrist pulse (Fig. 6a, inset),[49] indicating the high sensitivity of our sensor, showing great potential in real-time monitoring of human health. Then, we recorded the resistance variation of the sensor in response to air current (Fig. 6b). Stable and repeatable $\Delta R/R_0$ was observed, revealing excellent sensing performance for monitoring air pressure change. In addition, the sensor was also used to detect tiny muscle motion of face caused by puffing (Fig. 6c). Apart from small-scale motion detections, the pressure sensor can also be used for large-scale movement monitoring because of its high compressibility and excellent piezoresistive performance under large compressive strain. The pressure sensor was mounted on a finger and an elbow to monitor the bending motions. As shown in Fig. 6d and Movie S2,† a sensor was attached to the joint of an index finger to discern the bending degree of the finger. The resistance decreases rapidly upon joint bending and the $\Delta R/R_0$ increases with increasing bending angle. And the resistance change shows outstanding stability and reproducibility in slow and fast finger bending–release cycles. Fig. 6e and Movie S3† show a pressure sensor fixed on an elbow, stable and repeatable current signals were obtained during the elbow bending. And when the elbow bends quickly, a fast response of current signals follows. Finally, the sensor was adhered to the sole of a shoe to detect the electrical signals during walking and running. The sharp and stable sensing signals are shown in Fig. 6f. These results demonstrate that our PI/rGO pressure sensor is capable in large-scale movement monitoring, which can be used for emerging applications such as athlete training data acquisition systems, health monitoring, and artificial intelligence.

Conclusions

We have developed a unique flexible pressure sensor using PI/rGO composite aerogel. The superelastic and highly pressure-sensitive PI/rGO aerogels with aligned large aspect ratio honeycomb structure were fabricated using a bidirectional

freezing technique, which exhibit no significant plastic deformation and stress reduction after cyclic compression. The mechanical performance and electrical conductivity of the aerogels can be effectively tuned by changing the GO loading for different application requirements. Benefitting from their excellent mechanical robustness and novel aerogel structure, our sensors provide high pressure sensitivity (1.33 kPa^{-1}), high stability during cycling (1000 cycles), ultralow detection limit (3 Pa), broad detection range (80% strain, 59 kPa), fast response time (60 ms) and recovery time (70 ms). Remarkably, our aerogel sensors maintain stable and reproducible piezoresistive performance in a wide temperature range (at −50 °C, 100 °C, and 200 °C) in air, indicating promising applications in harsh environments. We have demonstrated various motions and pressure detections using our aerogel sensors, including wrist pulse, blowing, puffing, finger bending, elbow bending, walking, and running. Diverse applications of our aerogel sensors are expected in human health monitoring, artificial intelligence, artificial skin, etc.

Conflicts of interest

There are no conflicts of interest to declare.

Acknowledgements

References

1 Kenry, J. C. Yeo and C. T. Lim, *Microsyst. Nanoeng.*, 2016, **2**, 16043.
2 J. X. Wang, M. F. Lin, S. Park and P. S. Lee, *Mater. Today*, 2018, **21**, 508.
3 S. I. Rich, R. J. Wood and C. Majidi, *Nat. Electron.*, 2018, **1**, 102–112.
4 N. N. Jason, M. D. Ho and W. Cheng, *J. Mater. Chem. C*, 2017, **5**, 5845–5866.
5 W. Zhong, Q. Liu, Y. Wu, Y. Wang, X. Qing, M. Li, K. Liu, W. Wang and D. Wang, *Nanoscale*, 2016, **8**, 12105–12112.
6 X. Wang, L. Dong, H. Zhang, R. Yu, C. Pan and Z. L. Wang, *Adv. Sci.*, 2015, **2**, 1500169.
7 Y. Zang, F. Zhang, C. Di and D. Zhu, *Mater. Horiz.*, 2015, **2**, 140–156.
8 X. Chen, J. Shao, N. An, X. Li, H. Tian, C. Xu and Y. Ding, *J. Mater. Chem. C*, 2015, **3**, 11806–11814.
9 A. S. Dahiya, M. Francois, B. Sarah, N. Kevin, A. Daniel and P. V. Guylaine, *Adv. Mater. Technol.*, 2018, **3**, 1700249.

10 X. Pu, M. Liu, X. Chen, J. Sun, C. Du, Y. Zhang, J. Zhai, W. Hu and Z. L. Wang, *Sci. Adv.*, 2017, **3**, 1700015.

11 D. Kwon, T. I. Lee, J. Shim, S. Ryu, M. S. Kim, S. Kim, T. S. Kim and I. Park, *ACS Appl. Mater. Interfaces*, 2016, **8**, 16922–16931.

12 M. Kang, J. Kim, B. Jang, Y. Chae, J. H. Kim and J. H. Ahn, *ACS Nano*, 2017, **11**, 7950–7957.

13 C. Farcau, H. Moreira, B. Viallet, J. Grisolia, D. Ciuculescu, C. Amiens and L. Ressier, *J. Phys. Chem. C*, 2011, **115**, 14494–14499.

14 A. A. Barlian, W. T. Park, J. R. Mallon, A. J. Rastegar and B. L. Pruitt, *Proc. IEEE*, 2009, **97**, 513–552.

15 Y. Q. Li, Y. A. Samad and K. Liao, *J. Mater. Chem. A*, 2015, **3**, 2181–2187.

16 S. F. Zhao, G. P. Zhang, Y. J. Gao, L. B. Deng, J. H. Li, R. Sun and C. P. Wong, *ACS Appl. Mater. Interfaces*, 2014, **6**, 22823–22829.

17 Y. Qin, Q. Peng, Y. Ding, Z. Lin, C. Wang, Y. Li, F. Xu, J. Li, Y. Yuan, X. He and Y. Li, *ACS Nano*, 2015, **9**, 8933–8941.

18 J. Liu, H. B. Zhang, X. Xie, R. Yang, Z. S. Liu, Y. F. Liu and Z. Z. Yu, *Small*, 2018, **14**, 1802479.

19 H. Liu, W. Huang, J. Gao, K. Dai, G. Zheng, C. Liu, C. Shen, X. Yan, J. Guo and Z. Guo, *Appl. Phys. Lett.*, 2016, **108**, 011904.

20 H. Liu, M. Dong, W. Huang, J. Gao, K. Dai, J. Guo, G. Zheng, C. Liu, C. Shen and Z. Guo, *J. Mater. Chem. C*, 2017, **5**, 73–83.

21 N. Luo, Y. Huang, J. Liu, S. C. Chen, C. P. Wong and N. Zhao, *Adv. Mater.*, 2017, **29**, 1702675.

22 J. Huang, J. Wang, Z. Yang and S. Yang, *ACS Appl. Mater. Interfaces*, 2018, **10**, 8180–8189.

23 J. Y. Yang, Y. S. Ye, X. P. Li, X. Z. Lv and R. J. Chen, *Compos. Sci. Technol.*, 2018, **164**, 187–194.

24 X. D. Wu, Y. Y. Han, X. X. Zhang, Z. H. Zhou and C. H. Lu, *Adv. Funct. Mater.*, 2016, **26**, 6246–6256.

25 H. B. Yao, J. Ge, C. F. Wang, X. Wang, W. Hu, Z. J. Zheng, Y. Ni and S. H. Yu, *Adv. Mater.*, 2013, **25**, 6692–6698.

26 A. Tewari, S. Gandla, S. Bohm, C. R. McNeill and D. Gupta, *ACS Appl. Mater. Interfaces*, 2018, **10**, 5185–5195.

27 W. J. Huang, K. Dai, Y. Zhai, H. Liu, P. F. Zhan, J. C. Gao, G. Q. Zheng, C. T. Liu and C. Y. Shen, *ACS Appl. Mater. Interfaces*, 2017, **9**, 42266–42277.

28 Y. H. Wu, H. Z. Liu, S. Chen, X. C. Dong, P. P. Wang, S. Q. Liu, Y. Lin, Y. Wei and L. Liu, *ACS Appl. Mater. Interfaces*, 2017, **9**, 20098–20105.

29 B. Lv, X. T. Chen and C. G. Liu, *Sensors*, 2020, **20**, 1219.

30 D. J. Liaw, K. L. Wang, Y. C. Huang, K. R. Lee, J. Y. Lai and C. S. Ha, *Prog. Polym. Sci.*, 2012, **37**, 907–974.

31 I. Gouzman, E. Grossman, R. Verker, N. Atar, A. Bolker and N. Eliaz, *Adv. Mater.*, 2019, **31**, 1807738.

32 A. K. Geim, *Science*, 2009, **324**, 1530–1534.

33 S. Park and R. S. Ruoff, *Nat. Nanotechnol.*, 2009, **4**, 217–224.

34 X. Wang, Y. Y. Dai, J. Gao, J. Y. Huang, B. Y. Li, C. Fan, J. Yang and X. Y. Liu, *ACS Appl. Mater. Interfaces*, 2013, **5**, 8294–8299.

35 Y. Zhang, W. Fan, Y. Huang, C. Zhang and T. Liu, *RSC Adv.*, 2015, **5**, 1301–1308.

36 J. Y. Hong, B. M. Bak, J. J. Wie, J. Kong and H. S. Park, *Adv. Funct. Mater.*, 2015, **25**, 1053–1062.

37 X. Xu, H. Li, Q. Zhang, H. Hu, Z. Zhao, J. Li, J. Li, Y. Qiao and Y. Gogotsi, *ACS Nano*, 2015, **9**, 3969–3977.

38 A. M. Ektessabi and S. Hakamata, *Thin Solid Films*, 2000, **377**, 621–625.

39 X. C. Gui, J. Q. Wei, K. L. Wang, A. Y. Gao, H. W. Zhu, Y. Jia, Q. K. Shu and D. H. Wu, *Adv. Mater.*, 2010, **22**, 617–621.

40 M. Yang, N. F. Zhao, Y. Cui, W. W. Gao, Q. Zhao, C. Gao, H. Bai and T. Xie, *ACS Nano*, 2017, **11**, 6817–6824.

41 X. Wang, L. L. Liu, Z. L. Yu, X. W. Xu, Y. R. Zheng and S. H. Yu, *Angew. Chem., Int. Ed.*, 2015, **54**, 2397–2401.

42 R. P. Ren, Z. Wang, J. Ren and Y. K. Lv, *J. Mater. Sci.*, 2019, **54**, 5918–5926.

43 Y. N. Wang, Q. Y. Ge, X. L. Chen, S. L. Qi, G. F. Tian and D. Z. Wu, *Macromol. Mater. Eng.*, 2017, **302**, 1700082.

44 X. Y. Chen, H. Liu, Y. J. Zheng, Y. Zhai, X. H. Liu, C. T. Liu, L. W. Mi, Z. H. Guo and C. Y. Shen, *ACS Appl. Mater. Interfaces*, 2019, **11**, 42594–42606.

45 X. Zhao, W. L. Wang, Z. Wang, J. N. Wang, T. Huang, J. Dong and Q. H. Zhang, *Chem. Eng. J.*, 2020, **395**, 125115.

46 G. Ge, Y. C. Cai, Q. C. Dong, Y. Z. Zhang and J. J. Shao, *Nanoscale*, 2018, **10**, 10033–10040.

47 P. Sheng, *Phys. Rev. B: Condens. Matter Mater. Phys.*, 1980, **21**, 347–349.

48 P. Sheng, E. K. Sichel and J. I. Gittleman, *Phys. Rev. Lett.*, 1978, **40**, 1197–1200.

49 C. Pang, J. H. Koo, A. Nguyen, J. M. Caves, M. G. Kim, A. Chortos, K. Kim, P. J. Tok, J. B. Tok and Z. A. Bao, *Adv. Mater.*, 2015, **27**, 634–640.